Resistive wall mode active control physics design for KSTAR

Y. S. Park, S. A. Sabbagh, J. G. Bak, J. M. Bialek, J. W. Berkery, S. G. Lee, and Y. K. Oh
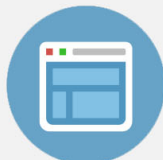
Resistive wall mode active control physics design for KSTAR

Y. S. Park,[1,a)] S. A. Sabbagh,[1] J. G. Bak,[2] J. M. Bialek,[1] J. W. Berkery,[1] S. G. Lee,[2]
and Y. K. Oh[2]
[1]*Department of Applied Physics and Applied Mathematics, Columbia University, New York 10027, USA*
[2]*National Fusion Research Institute, Daejeon 305-806, South Korea*

As KSTAR H-mode operation approaches the region where the resistive wall mode (RWM) can be unstable, an important issue for future long pulse, high beta plasma operation is to evaluate RWM active feedback control performance using a planned active/passive RWM stabilization system on the device. In particular, an optimal design of feedback sensors allows mode stabilization up to the highest achievable β_N close to the ideal with-wall limit, β_N^{wall}, with reduced control power requirements. The computed ideal $n = 1$ mode structure from the DCON code has been input to the VALEN-3D code to calculate the projected performance of an active RWM control system in the KSTAR three-dimensional conducting structure device geometry. Control performance with the midplane locked mode detection sensors, off-midplane saddle loops, and magnetic pickup coils is examined. The midplane sensors measuring the radial component of the mode perturbation is found to be strongly affected by the wall eddy current. The off-axis saddle loops with proper compensation of the prompt applied field are computed to provide stabilization at β_N up to 86% of β_N^{wall} but the low RWM amplitude computed in the off-axis regions near the sensors can produce a low signal-to-noise ratio. The required control power and bandwidth are also estimated with varied noise levels in the feedback sensors. Further improvements have been explored by examining a new RWM sensor design motivated by the off-midplane poloidal magnetic field sensors in NSTX. The new sensors mounted off of the copper passive stabilizer plates near the device midplane show a clear advantage in control performance corresponding to achieving 99% of β_N^{wall} without the need of compensation of the prompt field. The result shows a significant improvement of RWM feedback stabilization using the new sensor set which motivates a future feedback sensor upgrade. © 2014 AIP Publishing LLC. [http://dx.doi.org/10.1063/1.4862140]

I. INTRODUCTION

An important goal of KSTAR (Korea Superconducting Tokamak Advanced Research)[1,2] is to reach steady-state operation at high beta above the limits set by conventional ideal magnetohydrodynamic (MHD) stability. Recent advances in expanding the H-mode plasma operational space of the device marked substantial progress toward the ideal MHD no-wall beta limit, $\beta_N^{no-wall}$, which was computed and published for theoretical H-mode pressure profiles using the DCON code[3] as shown by the stability-relevant parameters, normalized beta versus internal inductance (l_i, β_N) in Fig. 1. The maximum sustained normalized beta, β_N, has exceeded 2.8 with plasma internal inductance, l_i, of 0.7, reaching β_N/l_i larger than 4,[4] where $\beta_N \equiv 10^8 \beta_t a B_0/I_p$ and $l_i \equiv \int B_p^2(r)d^3V/(V\bar{B}_p^2(1))$. Here, $\beta_t \equiv 2\mu_0\langle p\rangle/B_0^2$, V is the plasma volume and $\bar{B}_p$ is the average poloidal magnetic field on a flux surface as defined in Ref. 6. The $n = 1$ ideal MHD stability limits shown in Fig. 1 are evaluated in a manner that produces a realistic and conservative evaluation (relatively high value) of the β_N defining these limits. The internal profile parameters such as the pressure profile peaking and the minimum safety factor (q_{min}) are not known to high accuracy in present KSTAR equilibrium reconstructions, which rely on external magnetics alone.[5,7] Therefore, we have chosen a realistic

H-mode pressure profile shape, and q_{min} greater than, but close to unity (<1.5). Specifically, the β_N produced using this procedure is higher than if a more peaked pressure profile, and/or higher q_{min} were used. Even with this conservative calculation, the plasmas reach and exceed this limit in some cases. If the reconstructed equilibria are used directly to determine their ideal $n = 1$ no-wall stability, the greater pressure
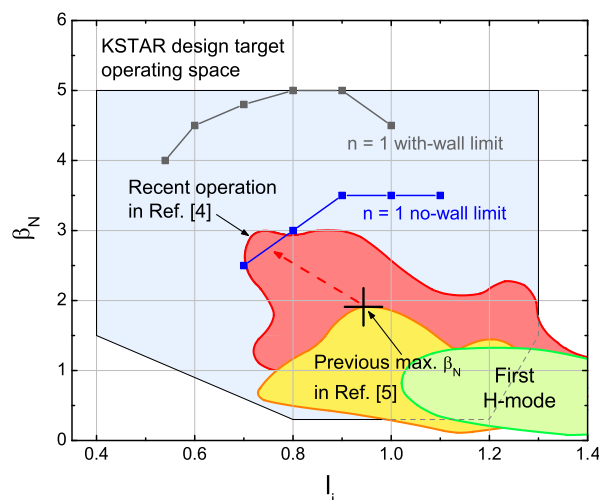

FIG. 1. KSTAR equilibrium operating space expansion toward the ideal MHD $n = 1$ no-wall limit computed using the DCON code. The design target operating space drawn is set by limits on the device poloidal field coils.[8]

a)Electronic mail: ypark@pppl.gov

peaking of the reconstructions produces a lower $n = 1$ no-wall stability limit β_N value, and a larger fraction of the plasmas are computed to be above this limit.

In plasmas exceeding the ideal no-wall limit, plasma current and pressure profiles can drive large scale global MHD instabilities such as the ideal kink/ballooning mode with low-n number (n denotes the toroidal mode number) which grows on the Alfvénic time scale, and the resistive wall mode (RWM) which grows much more slowly on the magnetic diffusion time scale of the penetration of the perturbed mode field through the surrounding resistive wall and other conducting structures, τ_w. The growth of the RWM typically leads to a major disruption of the plasma. Thus, developing a means to stabilize the RWM is crucial in devices aiming to operate significantly above the ideal MHD no-wall limit, as is planned for KSTAR.

The RWM can be stabilized either by passive or active means. Energy dissipation depending on plasma rotation and kinetic effects can stabilize the RWM,[7,9–18] however, this passive mode stabilization generally does not ensure full stabilization in all discharges, and active control of the RWM[16,18–34] is required for low disruptivity at high normalized beta. The growing $n = 1$ RWM, which is a significant concern in advanced tokamak fusion plasmas, can be either non-rotating or slowly spinning (rotation frequency $\sim O(1/\tau_w)$). In active RWM stabilization, control coils and sensors are used to track and reduce the perturbed $n = 1$ mode field. Two proposed feedback logics for magnetic control are the "Smart Shell" (Ref. [19]) and "Mode control" (Ref. [23]) where the former uses the total measured field to be cancelled by feedback, while the latter explicitly cancels only the magnetic perturbation from the mode by first compensating the external field from the measured sensor signals. With active feedback applied, the mode can be converted to a rotating global kink/ballooning mode that is stabilized by faster rotation ($>1/\tau_w$) which can significantly reduce the disruption probability.[16] The existing segmented in-vessel control coils (IVCCs)[35] in KSTAR with various magnetic field sensors can potentially provide active $n = 1$ RWM control in the device. In the present work, the three-dimensional (3D) VALEN-3D code[36] is used to analyze the effectiveness of various feedback sensor designs to optimize the performance and reliability of active RWM control to sustain continuous high β_N plasma operation in KSTAR.

II. UNSTABLE EIGENMODES AND RWM SENSORS

The most unstable $n = 1$ eigenfunction computed from a theoretical KSTAR equilibrium having $l_i = 0.7$ and $\beta_N = 5.0$ with an H-mode pressure profile is used to model the plasma mode to control, and is combined with the 3D finite element conducting structure in the VALEN feedback analysis. The perturbed mode structure is assumed to be rigid and can rotate toroidally. Figure 2 shows the poloidal variation of the perturbed normal field for the unstable $n = 1$ mode from DCON used in the calculations. The inclusion of multiple plasma modes either with multiple toroidal mode numbers, or with $n = 1$, may be needed if the secondary or higher modes have a dominant plasma response as computed by the ideal MHD stability functional for each mode (computed by an ideal MHD code, such as the DCON code). For the analysis conducted here, secondary and higher modes are sub-dominant, and hence their exclusion in these computations is valid. The second and third least stable modes with $n = 1$ are shown in Fig. 3. Examining several toroidal phases of the mode, it is clear that the relative amplitude is largest on the low field side (large R), showing the ballooning characteristic of the mode. The mode amplitude remains significant at lower R values until the divertor region is reached, and decreases significantly at lowest radial points. The amplitude of the secondary modes remains significant at poloidal angles on the large major radius side (outboard side), reaching the divertor region. The mode amplitude is significant in the divertor region itself. The mode eigenfunction depends on equilibrium parameters such as plasma current and pressure, and is chosen as the most unstable eigenvector predicted with the highest growth rate close to the ideal with-wall limit shown in Fig. 1.[3]

Figure 3 also illustrates the two-dimensional geometry of the KSTAR conducting structure including passive stabilizer plates and IVCCs along with the magnetic sensors[37] analyzed. The design of the existing copper passive stabilizing plates in KSTAR was determined by considering its impact on RWM passive growth rates.[3,7] The passive plates are positioned to effectively couple to RWMs which are ballooning in nature with the highest mode perturbation on the outboard side. Each of the up-down symmetric stabilizers is segmented into four toroidal quadrants, and connected by gap resistors to produce a toroidal resistance accommodating controllability of both vertical instabilities ($n = 0$) and
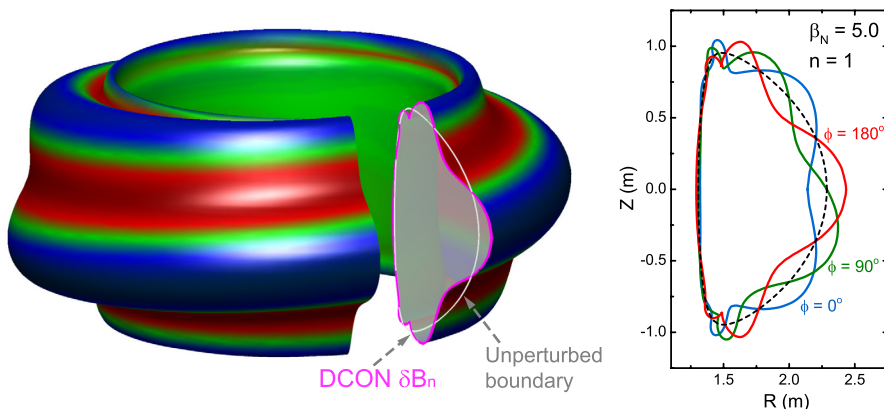
FIG. 2. DCON computed perturbed B-normal field for the unstable $n = 1$ eigenfunction used in the analysis. On the left, color scale is from red (negative) to green (approx. zero) to blue (positive). Perturbations at different toroidal phases are drawn on the right. The perturbed normal field amplitude shown has been exaggerated to clarify the mode shape.
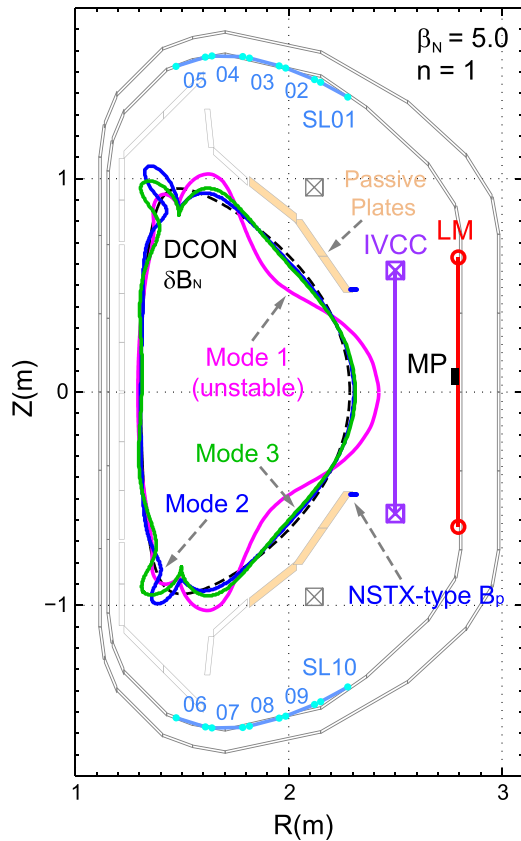
FIG. 3. Two dimensional view of KSTAR conducting structure including RWM control coil, sensors, and the analyzed *B*-normal field distribution of the unstable eigenfunction (mode 1). Here, IVCC denotes in-vessel control coil, LM sensors, SL sensors, and MP.

RWMs ($n = 1$). The RWM sensors can have different impact on control performance depending on various aspects, such as their spatial distribution, proximity to the RWM eigenfunction, the orientation of the magnetic perturbation measured, and magnetic coupling to induced currents in conducting structure and to the applied control field. In this study, the following device sensors are analyzed to investigate how the different sensor characteristics affect the RWM control physics, and to determine the best sensor set for RWM control: (i) the locked mode (LM) sensors—which approximately measure the normal field perturbation on the

outboard midplane directly facing the mode, (ii) the saddle loop (SL) sensors—off-midplane poloidal field sensors behind the passive stabilizing plates, (iii) the Mirnov probes (MPs)—small pickup coils measuring poloidal field at the outboard region, and (iv) NSTX-type sensors[16]—poloidal field sensors proposed to enhance control performance. In Sec. III, the magnetic stabilization system to be used for RWM active control in KSTAR is described using the full 3D details of the magnetic sensor sets above. Section IV examines the expected control performance of the candidate device sensors and compares theoretical RWM growth rates computed by using the different sensor sets. RWM control power requirements using the determined optimal sensor sets are addressed in Sec. V. A further improvement in control performance can be achieved by implementing a new sensor design and Sec. VI illustrates its advantage over the present sensors. Conclusions are presented in Sec. VII.

III. RWM CONTROL ACTUATORS AND 3D CONTROL MODELLING

A primary requirement in the modeling of the planned RWM active control system on KSTAR is a 3D model of the device conducting structure, sensors and actuator coils. The VALEN-3D code implements a general circuit formulation and uses a finite element representation of the conducting wall in an integral formulation to model arbitrary conducting elements and a representation of stable and unstable plasma modes in 3D.[36,38] The code models the external magnetic properties of a plasma mode as the normal component of the magnetic perturbation at the unperturbed plasma surface, and the mode interaction with surrounding conductors is represented by a scalar plasma permeability. The code allows various feedback systems including magnetic sensors and active control coils to be evaluated via transient simulation and eigenvalue analysis. The VALEN-3D model for KSTAR, shown in Fig. 4, comprises nearly 8000 circuit equations of segmented conducting elements for a realistic description of the complex device geometry. This number of circuit elements in the KSTAR model is more than adequate to properly resolve the control of the plasma modes considered. For comparison, earlier studies of other devices such as the DIII-D tokamak used models segmented into ~1400 elements and
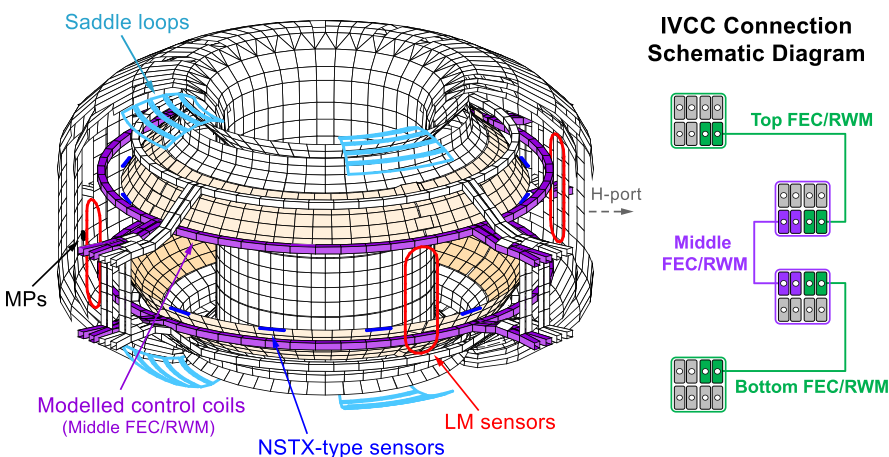

FIG. 4. KSTAR conducting structure including copper passive stabilizer plates (displayed in yellow) and middle IVCCs and the present device sensors comprises 4 LM sensors, 40 SL sensors, 3 MPs, and imagined 24 NSTX-type sensors for active $n = 1$ RWM control implemented in the VALEN-3D finite element model. The computational model of the middle IVCCs displayed includes the stainless steel coil casings surrounding the copper coils. A schematic diagram on the right shows the electrical connection of the IVCC elements.

the HBT-EP tokamak which used a model consisting of ~6400 elements[36] due to its fairly complex passive stabilizing conducting structures specialized for RWM control studies.

The uniquely designed IVCC assembly comprises four poloidal positions with four toroidal quadrants for each poloidal position (total 16 segments) to generate a dominant *n*-spectrum of applied magnetic field up to 2. As is shown in a schematic diagram in Fig. 4, each IVCC segment has 8 insulated copper conductors which can be independently connected to form various axisymmetric/non-axisymmetric coil configurations. The IVCCs are surrounded by a 3 mm thick stainless steel coil casing which shields high frequency AC fields and produces a small decrease in RWM control performance. The rotating field generated by the top and bottom field error correction (FEC)/RWM coils can be significantly shielded by the nearby conductive stabilizer plates and is therefore not as strongly coupled to the RWM. Thus, the middle FEC/RWM coils (four toroidal quadrants each having two turns) are considered as the most probable RWM control actuator. The middle FEC/RWM coils are also beneficial to effectively produce the control field on the outboard midplane region where the strength of the unstable RWM is strongest. The unloaded circuit parameters for each coil quadrant, $L = 44\,\mu H$, $R = 3.66\,m\Omega$ with $L/R = 12\,ms$ are calculated values in the VALEN-3D for the modeled coils, and used as default circuit parameters in the rest of this study. To examine an actuator circuit faster than the RWM growth rate analyzed ($\gamma_{RWM}^{-1} > 1\,ms$) which would produce higher control performance, $L = 44\,\mu H$, $R = 44\,m\Omega$ with $L/R = 1\,ms$ are used by adding resistance to the circuit.

The frequency response and phase lag of the active feedback system with the effect of the vacuum vessel and passive plates included are calculated describing the 3D model as a set of coupled equations,

$$[L]\left\{\frac{dI(t)}{dt}\right\} + [R]\{I(t)\} = \{V(t)\} = \{V_0\}^{i\omega t},$$
$$\{I(t)\} = \{I_0\}^{i\omega t}, \tag{1}$$
$$\{I_0\} = [[L](i\omega) + [R]]^{-1}\{V_0\}.$$

Here, the square brackets represent matrices, {} represents a column vector, and ω defines the voltage driving frequency comprising the system of approximately 8000 equations. In the calculation, alternating voltage is applied to all four control coils with an $n = 1$ configuration. The resulting attenuation of the control coil current amplitude and phase lag as a function of driving frequency are shown in Fig. 5. The unloaded coil shows higher attenuation and phase lag at lower frequency compared to the coil with lower L/R time. The current amplitude reduces to half of its original value at 24 Hz driving frequency with phase lag of 56°, while corresponding values for the faster coil are 350 Hz and 47°. The result indicates that the control field produced by the unloaded coils is strongly limited in its operating frequency, and if the RWM rotates faster than the given coil response, both reduced control field magnitude and phase lag larger than the stable feedback phase window of the control system
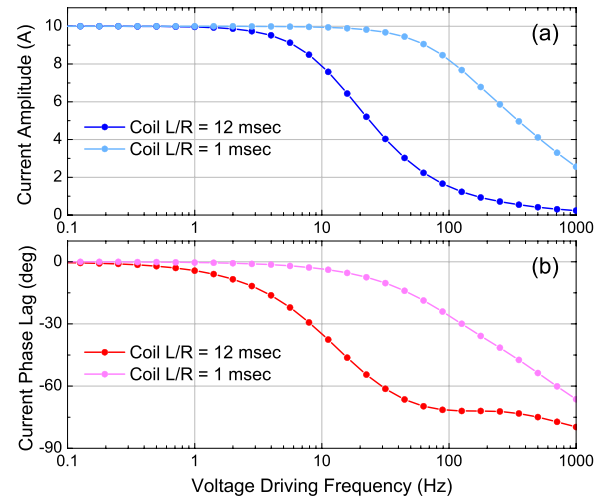

FIG. 5. Comparison of control coil current amplitude and phase lag as a function of control voltage frequency for different coil circuit parameters.

can preclude mode stabilization and a loaded coil circuit with higher power supply capability will be needed. Actuators having faster response are generally more advantageous for RWM feedback, however, the choice of feedback sensors and their positions can change the requirements for the fast coil response. This is addressed in Secs. IV–V.

IV. ACTIVE RWM FEEDBACK DESIGN AND PHYSICS ELEMENTS AFFECTING CONTROL PERFORMANCE

In the VALEN-3D calculations, the strength of the instability[36,38] is varied to calculate the RWM growth rate and the associated eigenvector including the influence of the conducting structure at different values of β_N. The feedback control calculations use power supply voltage control in the VALEN model, and sensor signals in the control logic determine the voltage applied to the RWM control coils. A proportional gain controller has been used with an ideal control system assumption in the study. The feedback phase (δ_{FB}), a relative phase difference between the toroidal phase of the total measured field by the sensors (δ_{sensor}) and the phase of the mode at the outboard midplane where control coils are located ($\delta_{FB} = \delta_{CC} - \delta_{sensor}$), is determined at an intermediate value of $\beta_N = 3.9$ between the ideal no-wall and with-wall limits and applied as a fixed constant over the full range of β_N. Figure 6 shows the determination of the feedback phase from the computed $n = 1$ mode flux measured by different feedback sensors. The LM sensors measure the same toroidal mode phase as the control coils, so the applied control field can directly oppose the mode perturbation by using the sensor set via negative feedback applied with zero phase difference unlike the off-midplane SL sensors which require a compensation of the difference in the measured mode phase. The range of the stable feedback phase found using this approach is typically sufficient to provide stabilization over the range of β_N considered although this results in a slightly unoptimized control performance.

Another primary aspect of the analysis is the choice of the 3D sensors used in the feedback modeling. A good feedback sensor should have strong coupling to the RWM. In
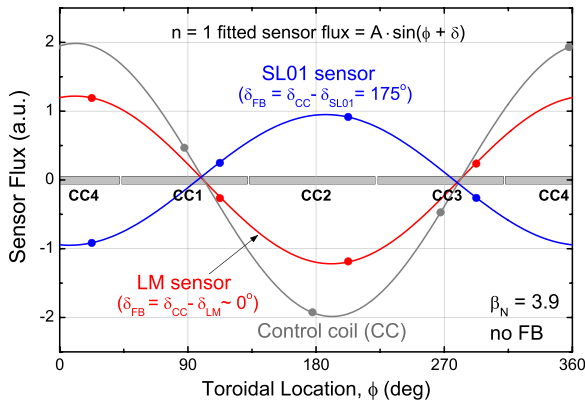
FIG. 6. Computed $n = 1$ perturbed flux measured by feedback sensors and coils, and determined feedback phases. Here, the toroidal angle is counter-clockwise from the device port H shown in Fig. 4. Regions displayed in grey denote the toroidal extent of the four control coils. The measured flux from each sensor set is scaled for clear comparison.

FIG. 7. Theoretical feedback performance using the LM sensors. RWM growth rate is plotted versus β_N. The computed feedback improvements expected from external field compensations are shown.

KSTAR, sensors proximate to the outboard midplane region of the plasma would be advantageous in this regard. Second, the impact of the external field produced by actuators and induced currents on conducting structures should be minimized. This becomes critical if the applied field measured by the sensors has the same component of the mode perturbation field. The field from induced currents in the conducting structure cannot be easily compensated and so is more deleterious. Different physics aspects of the implemented device sensors which influence the feedback performance are analyzed in this section.

A. Midplane radial field sensors strongly coupled to applied control fields and induced vessel currents

The four midplane LM sensors are located poloidally where the ballooning structure of the unstable $n = 1$ eigenfunction is strongest, and would appear suitable to provide control at high β_N. However, the control performance using this sensor set has been found to be strongly limited since the sensors are strongly coupled to the applied field produced by the control coils and induced currents on the wall. The LM sensors have a single turn with an area of 0.46 m^2, and measure radial field perturbations at the inside of the inner vacuum vessel wall. The performance of the LM sensors is shown in Fig. 7. The RWM growth rate calculation
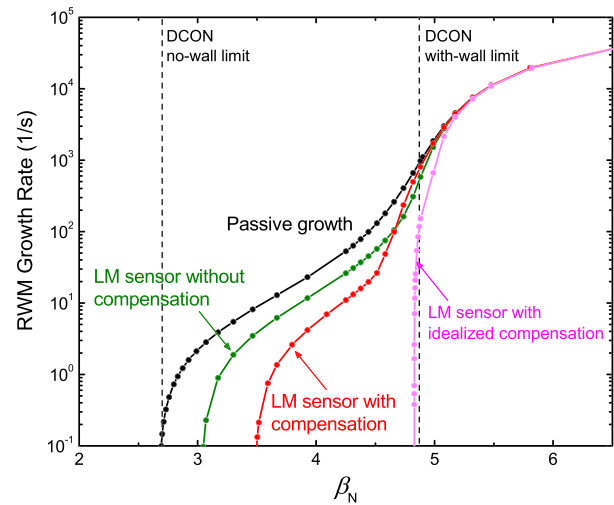
using the VALEN-3D code showed that the mode can be stabilized only up to $\beta_N = 3.0$ due to the strong mutual coupling of the sensors to the applied control field and the vessel wall, yielding a fairly low obtainable $C_\beta = 16\%$ of the $n = 1$ ideal with-wall limit. Here, $C_\beta = (\beta_N - \beta_N^{no-wall})/(\beta_N^{wall} - \beta_N^{no-wall})$. Note that the applied proportional feedback gain, G_p, is varied to produce the highest possible C_β in the calculations. The control performance is improved by compensating the applied field component from the LM sensors corresponding to increased C_β of 37% (stabilization up to $\beta_N = 3.5$). It is found that the control performance is additionally limited by feedback-induced vessel current circulating around the elongated horizontal port penetrations facing the LM sensors. Figure 8 shows the induced vessel currents flowing around the LM sensors during the VALEN feedback calculation and a picture of the LM sensors installed in the device. A comparison of the computed flux measured by theoretical, ideal B_p and B_r sensors most closely positioned to the mode at the outboard midplane is shown in Fig. 9. Only the prompt applied field from the control coils is compensated in the LM sensors (displayed by the red solid line). The measured $n = 1$ phase of the ideal B_r sensors represents the correct toroidal mode phase that the
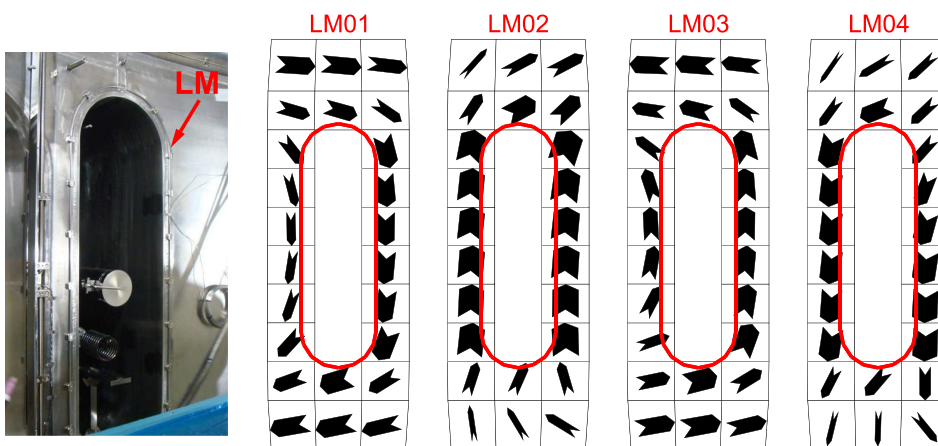

FIG. 8. A picture of the LM sensor surrounding the port penetration in the KSTAR outboard inner vessel wall (left), and induced vessel currents produced during feedback in the VALEN-3D calculation.
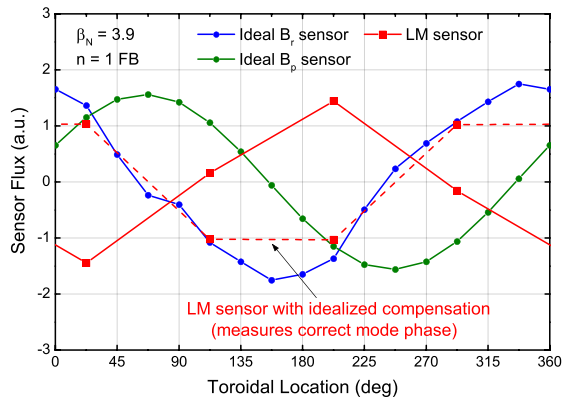
FIG. 9. Computed magnetic flux from the idealized sensors and the LM sensors to measure $n = 1$ mode amplitude and phase when feedback is applied.

LM sensors should equally measure since they are both midplane sensors. However, the perturbed B_r field produced by the induced vessel currents strongly alters the field measured by the LM sensors and consequently, the LM sensors in the calculation do not track the correct mode phase identified by the ideal B_r sensors. The LM sensors with idealized compensation of the vessel current (displayed by the red dotted line) measure the same phase as the ideal B_r sensors. The measured phase of the ideal B_r sensors shows a minor perturbation due to its higher mutual coupling to the external field than the ideal B_p sensors. As shown in the time domain feedback calculation in Fig. 10, this added perturbation from the induced vessel current eventually leads to failure in feedback by loss of mode phase tracking. Note that this comparison is meant only for illustration since this idealized compensation is not practically possible. Other sensor sets should be prepared for RWM control to circumvent the limitations of the LM sensors.

B. Off-midplane saddle loops for RWM control

The SLs are positioned near the top and bottom of the vacuum region and are somewhat behind the internal conducting structures including the conductive passive
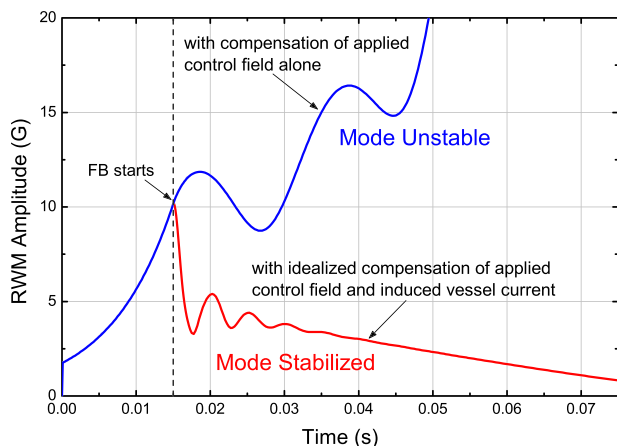

FIG. 10. Comparison of active feedback control with and without compensation of the induced vessel current from the LM sensors. Feedback calculation is performed at $\beta_N = 4.5$ which is above the highest β_N achievable in the case when only the applied control field is compensated ($\beta_N = 3.5$) in Fig. 7.

stabilizing plates (Fig. 3) which could curtail the magnitude of the mode perturbation measured by the sensors. The SL sensors have a single turn and an area of 20.4 e-2 m^2 for the largest loops SL01/10, and 13.4 e-2 m^2 for the smallest loops SL05/06. The 40 (10 poloidal positions for four 90° separated toroidal positions) off-midplane SL sensors are included in the VALEN-3D model and the modeled 3D geometry of these sensor sets is shown in Fig. 4. Compared to the LM sensors, a smaller coil-to-sensor coupling and the absence of nearby port penetrations can potentially provide better control. The mutual coupling between the SL01/10 sensor and the closest control coil quadrant is only ~9% of that of the LMs. Since the SLs at the toroidal position shown in Fig. 3 are distributed along different poloidal locations, the control effectiveness of the sensors can be altered by their proximity to the unstable RWM eigenfunction and also by the effect of the conductive passive plates. The latter becomes significant when the mode is highly unstable or rotates toroidally.

To evaluate the effectiveness of the SLs in the presence of the passive plates, the measured sensor signals are calculated from the VALEN-3D eigenmodes as shown in Fig. 11. The RWM has a growth rate (γ_{RWM}) of 23 s^{-1} without feedback applied, and the sensor signals are calculated and compared between cases with and without the sensor mutual coupling to the passive plates. Among the 5 up-down SL pairs at the same major radii, the SL05/06 measures the lowest $n = 1$ amplitude and the outermost SL01/10 sensors measure about 30% higher perturbation than the SL05/06 pair. This can be explained by the mode strength increasing closer to the outboard midplane as shown in Fig. 2 (Fig. 3). The case without the sensor coupling to the passive plates shows that the magnitude of mode perturbation shielding by the passive plates is higher towards the outer SLs, however, the corresponding change in mode helicity, determined as the difference between the mode phase measured by the toroidal SL arrays above and below the midplane shown in Fig. 11(b), is significant towards the inner SLs, and the SL05/06 pair is found to experience the highest helicity change. Although the input unstable mode eigenfunction is rigid, the response of the conducting structures changes the measured helicity of the total measured field (mode + wall currents) in the calculations. The smaller amplitude of the local perturbation field at the inner SLs makes these sensors more prone to measure the mode phase incorrectly although the absolute magnitude of the passive plate shielding effect is smaller than that in the outer SLs. Additional calculations prove that this significant change of the mode helicity in the inner SLs becomes stronger with higher mode growth rate which results in a higher inductive response of the passive plate currents. This indicates that in stabilization using the inner SLs, the feedback phase might be corrected for a given mode growth which could eventually make feedback more difficult.

The RWM control performance is examined for all SL sensor pairs. Consistent with the analysis shown in Fig. 11, the innermost SL05/06 exhibits the lowest value of obtainable $C_\beta = 32\%$ (Fig. 12) which is slightly lower than the performance of the compensated LM sensors. The SL04/07 pair is found to stabilize the mode up to $C_\beta = 69\%$ with applied field compensation, as summarized in Table I, along with the
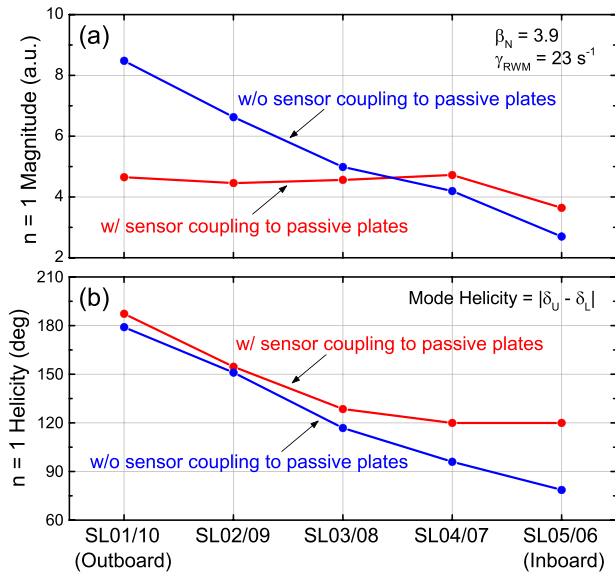
FIG. 11. (a) RWM amplitude measured by different SL sensor sets calculated with and without the sensor mutual coupling to the conductive passive plates, and (b) mode helicity. Here, the mode helicity is defined as an absolute difference between the mode phase measured by the SLs above (δ_U) and below (δ_L) the midplane.

TABLE I. The highest achievable β_N and corresponding C_β by stabilization using different device sensor sets and control coil circuit times. The applied control field is compensated from the sensors.

		LM	$SL_{01/10}$	$SL_{02/09}$	$SL_{03/08}$	$SL_{04/07}$	$SL_{05/06}$
Coil L/R	β_N	3.5	4.6	4.0	3.8	4.2	3.4
= 12 ms	C_β	37%	86%	61%	52%	69%	32%
Coil L/R	β_N	3.1	4.0	3.5	3.5	3.7	3.5
= 1 ms	C_β	21%	62%	38%	37%	47%	36%

Feedback using the fast coil circuit is generally expected to exhibit better performance over a slower circuit. However, the inductive shielding of the mode field by the passive plates can be more significant when using the fast coil, and combined use with the SL sensors which are highly affected by the passive plates can potentially result in degraded control. Additional calculations with the fast control coil circuit with loaded coil resistance ($L/R = 1$ ms) and an increased feedback gain show that the fast coil action is not beneficial to improve control performance when it is used with the examined feedback sensors. In the calculations, the conducting structure excites a very slowly growing ($\gamma_{RWM} \sim 10$ s^{-1}) secondary instability due to the applied feedback which limits the performance using the fast control coil. Figure 13 shows the real and imaginary parts of the unstable eigenvalues according to different feedback phases applied to the feedback relation between sensors and control coils (Fig. 6). The real and imaginary part of the eigenvalues show mode growth rate and rotation, respectively. It is shown by the calculations that the optimal feedback phase for the fast control coil is shifted by $\sim 10°$ from the value derived from the mode eigenvalue analysis indicating the effects from the higher eddy current. The secondary instability is found to be excited when the feedback phase is applied to stabilize the RWM and its eigenfunction is found to have a similar $n = 1$ induced current distribution on the passive plates. Because of the onset of a secondary eigenmode having a small growth rate and rotation, the feedback with the fast control coil has
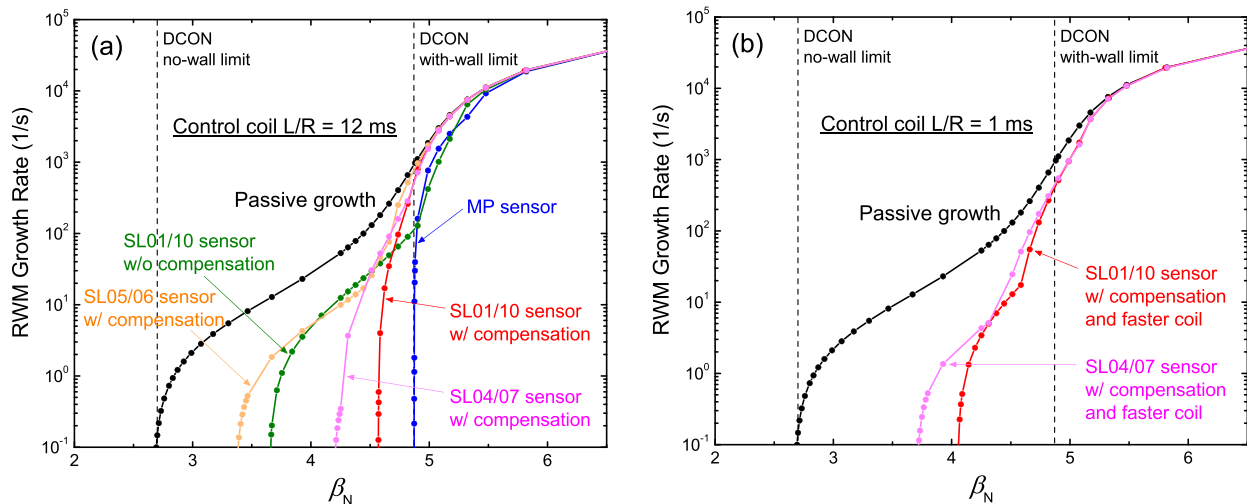
other SL pairs. Unlike the LM sensors, vessel current near the SL sensors does not significantly limit the control performance, and compensation of the applied control field alone can increase the C_β from 44% to 86% for the SL01/10 sensors which is the highest performance among the SL sensor sets examined. The higher performance of the SL01/10 over the SL04/07 is thought to be due to a change in response of the conductors by applied feedback which may perturb the inner SL measurement more strongly. In addition, the short wavelength of the perturbed mode field in the divertor region could make mode phase identification more difficult than in the outer region near the SL01/10 sensors. A fast coil circuit is beneficial for feedback with a high actuator frequency as shown in Fig. 5 and is required to control modes with fast growth rates and that rotate quickly.

FIG. 12. RWM growth rate vs. β_N with different SL and MP sensor sets. The computed feedback performance change by prompt applied field compensation and control coil circuit parameters are shown in (a) with unloaded coil and (b) with faster coil response.
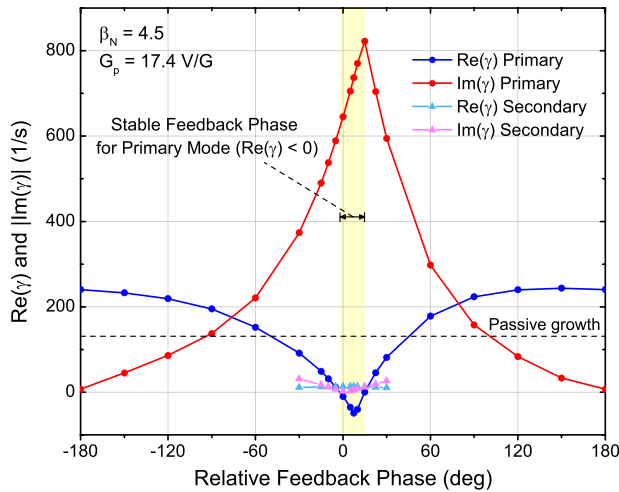
FIG. 13. RWM amplitude and phase during feedback stabilization using the SL01/10 sensor sets (8 total) and the fast control coil circuit. The region highlighted in yellow is a stable feedback phase window where the primary mode is stabilized.

an achievable C_β of 62% for SL01/10 and 47% for SL04/07 which are lower than the value with the unloaded coil circuit as shown in Fig. 12. This secondary mode could be controlled by using dual component sensor feedback as successfully demonstrated in NSTX.[16,18]

V. PROJECTED RWM CONTROL POWER REQUIREMENTS

Power requirements for RWM stabilization are calculated from time domain feedback control calculations using the compensated SL01/10 sensors which showed the highest control performance among the examined LM and SL sensors. Using both the unloaded and fast control coil circuits, feedback is started when the growing mode amplitude becomes 10 G ($\delta B_{RWM}/B_{T0} = 0.06\%$) and the mode starts to rotate and is then fully suppressed by the feedback as shown in Fig. 14. The RMS control power is calculated for different values of β_N with corresponding C_β of 42%–86% with the unloaded control circuit. The target RWM has a growth rate of 11.5–149.7 s^{-1} in the range of β_N examined. Corresponding values for the fast control circuit are $C_\beta = 14\%$–62% and $\gamma_{RWM} = 2.2$–30.7 s^{-1}. Feedback gains are chosen to apply the same initial control voltage to modes having different growth rates, $|\tilde{V}_0| = 0.7$ V/turn to the unloaded control circuit and

7 V/turn to the faster circuit, and the RMS power is calculated over a time interval required to stabilize the mode below 2 G amplitude. The resulting control time interval is between 51 and 131 ms (355–450 ms using the faster circuit) which correspond to several mode growth times. The required control power for the entire middle-IVCC coil set in Fig. 15 shows a non-linear dependence on β_N. The control power sustains $\sim$140 W level ($\sim$1.2 kW using the fast circuit) and rapidly increases as β_N approaches the control limit of the feedback sensors (Fig. 12) above which the control is lost. The transient peak control power (P_{max}) using the unloaded circuit occurs between 280 and 335 W for the entire coil set. The peak values of the required coil currents and voltages (I_{max}, V_{max}) are less than 338 A-turn and 0.7 V/turn for each coil. The mode rotates faster under applied feedback as it becomes more unstable at higher β_N and the highest voltage control bandwidth (f_{max}) is 36 Hz in the calculation, however, requirements can surpass these idealized values if the mode rotates faster than the calculation indicates which could eventually require a faster control coil circuit and correspondingly higher feedback gain. The calculations using the faster control circuit in the figure show higher control power requirements due to the loaded coil resistance with $P_{max} = 9.5$ kW, $I_{max} = 880$ A-turn, $V_{max} = 11.2$ V/turn, and $f_{max} = 92$ Hz.

To estimate the control power requirement in the presence of non-ideal effects, Gaussian "white" noise is included in the SL01/10 sensors. The effects of both high and low frequency noise are examined. The high frequency noise chosen ($f_{noise} = 10$ kHz) is representative of modes rotating at typical plasma rotation speeds, while the lower frequency chosen ($f_{noise} = 1$ kHz) is at the high end of the frequency range for RWM activity. For both the unloaded and the fast control coil circuits, stabilization is calculated at C_β which is 20% lower than the maximum value reached by each coil circuit. For the unloaded coil, $G_p = 2$ V/G and an unstable mode eigenfunction at β_N of 4.1 ($C_\beta = 66\%$) having $\gamma_{RWM} = 36.4$ s^{-1} are used, and corresponding values for the calculation with the fast coil are $G_p = 17.4$ V/G, $\beta_N = 3.6$ ($C_\beta = 42\%$) with $\gamma_{RWM} = 11.5$ s^{-1}, respectively. Figure 16 shows the increase in required control power with increasing sensor noise level and different control circuit response times and noise frequencies. The noise level shown is the RMS noise magnitude relative to the highest mode amplitude measured by the sensors when the feedback is started (Fig. 14(a)). With the unloaded control coil circuit, the feedback can stabilize the unstable mode even with the applied sensor
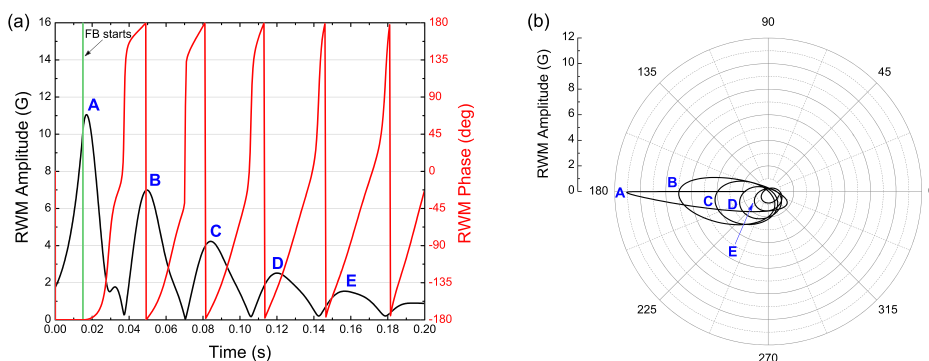

FIG. 14. (a) RWM amplitude and phase during feedback stabilization at $\beta_N = 4.5$ using the SL01/10 sensor sets (8 total) and the unloaded control coil circuit. The control time required to stabilize the mode amplitude below 2 G is 114 ms in the calculation. (b) Polar plot of RWM amplitude and phase during feedback.
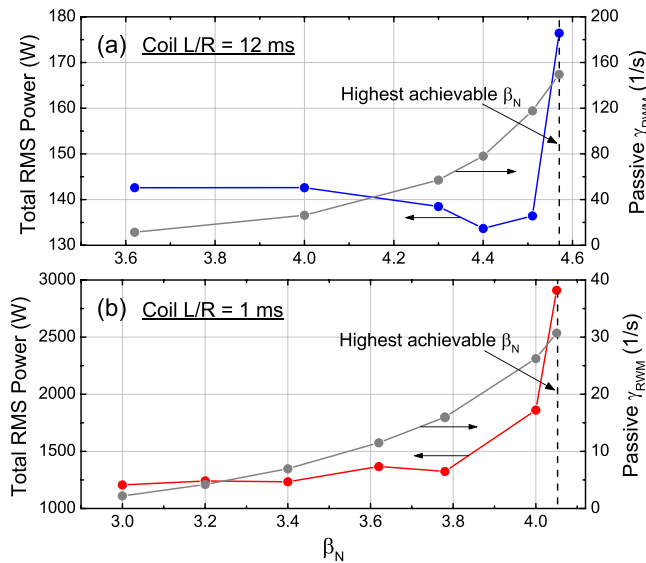
FIG. 15. RWM passive growth rate at different β_N and total RMS control power required to stabilize the mode (a) with the unloaded control coil circuit and (b) with faster coil response.

noise magnitude a few times higher than the peak mode amplitude measured by the sensors. The required control power stays at a modest level up to $\sim 2\,\text{kW}$ but when the relative noise magnitude becomes greater ($\delta B_{noise}/\delta B_{RWM} > 5$ with $f_{noise} = 10\,\text{kHz}$ and a lower threshold with $f_{noise} = 1\,\text{kHz}$), the mode is metastable and the mode amplitude cannot always be sustained below its initial value. It should be noted that the calculated magnitude of the mode field measured by the SL01/10 sensors is weak (at $\beta_N = 4.1$, the SL01/10 measures $n = 1$ field amplitude that is only $\sim 2\%$ of the ideal B_p sensor measurement) hence the absolute magnitude of the tolerable sensor noise level is much smaller than for idealized sensors
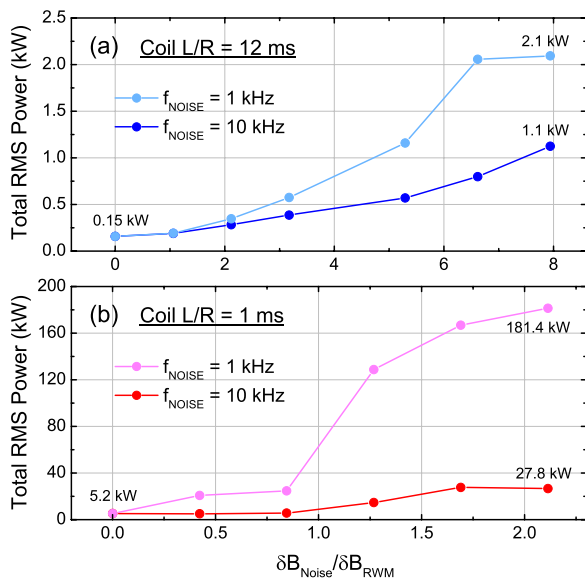

FIG. 16. Total RMS control power versus sensor white noise level relative to the peak $n = 1$ mode amplitude measured by the SL01/10 sensors. (a) Feedback using the unloaded coil at $\beta_N = 4.1$ with $G_P = 2\,\text{V/G}$ and (b) using faster coil response at $\beta_N = 3.6$ with $G_P = 17.4\,\text{V/G}$.

closely positioned to the mode. In the calculations, the feedback using the unloaded coil allows only a $2\,\text{G}$ absolute noise level in the SL01/10 sensors which can be compared to a $10\,\text{G}$ noise level allowed in the case with the ideal B_p sensors.[7] The tolerance to sensor noise varies with the response time of the feedback. By using the fast control coil response, the control is easily lost at small noise levels which result in a higher increase in the required control power. The control power increase is significant when the noise frequency becomes lower. The required control power using the fast coil response reaches over $180\,\text{kW}$ with $f_{noise} = 1\,\text{kHz}$, and the requirements could be greater with a higher noise amplitude. The limited control performance of the SL sensors due to measurement noise suggests the implementation of a new RWM sensor design which is discussed in Sec. VI.

VI. FEEDBACK IMPROVEMENT BY NEW RWM SENSOR DESIGN

Similar to the LM sensors, the MPs shown in Fig. 3 are located where the strength of the mode perturbation is strong, and measure the poloidal field component of the mode which can minimize coupling to the field applied from the control coils and circulating eddy currents in the wall. The MPs have 88 turns and a small area of $5\,\text{e-4 m}^2$ for measuring poloidal field at 3 different toroidal locations. Among all of the MPs located along the poloidal circumference of the inner vessel wall, the sensors closest to the midplane are chosen. The calculated performance of the MPs is presented in Fig. 12(a). The advantages of the MPs result in greater control, almost up to the with-wall limit in the ideal case. However, the limited toroidal distribution of the MPs and the small sensor area would make this sensor impractical to measure perturbed magnetic flux at very low frequency in an actual RWM control environment with low signal to noise. Therefore, the MPs are more appropriately used for complementary measurement of poloidal field perturbations.

A new RWM feedback sensor design is considered in the KSTAR VALEN model which yields improved control performance. The design is motivated by the existing sensor set on NSTX[31] which has successfully demonstrated active $n = 1$ control with six midplane control coils in the device by measuring the poloidal component of the RWM.[16] The width and length of the rectangular-shaped B_p sensors are $0.028\,\text{m}$ and $0.28\,\text{m}$ (area $= 7.8\,\text{e-3 m}^2$), respectively, with 44 turns. Twenty four total sensors (12 for each toroidal sensor array above and below the midplane) are located at the outermost tip of the copper passive stabilizer plates as shown in Fig. 3. This sensor configuration can provide a reliable measurement of the RWM phase in the region where the mode strength is significant with reduced inductive coupling to the passive plates and the vacuum vessel. The computed mode amplitude measured by the sensor (G/turn) is ~ 40 times higher than the SL01/10 which yields successful stabilization even with higher measurement noise. The greater number of toroidal sensors can also measure higher n resonant field components, which is an important tool for the study of multi-mode RWMs. Figure 17 shows the expected increase in performance by using the new sensor set. Due to the
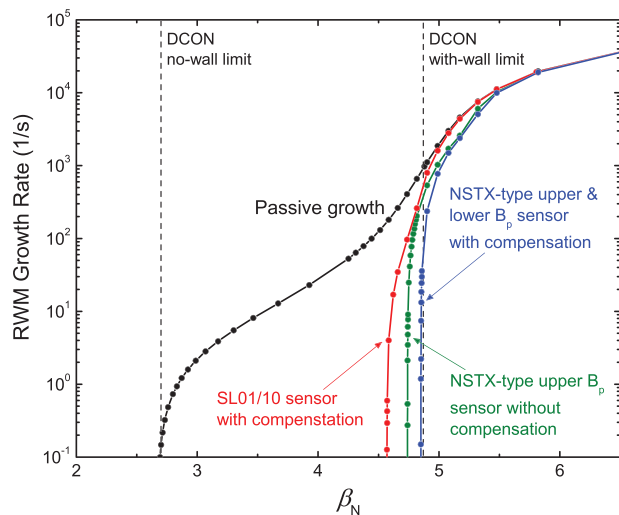
FIG. 17. RWM growth rate vs. β_N with different NSTX-type B_p sensor sets (upper toroidal array vs. upper and lower toroidal arrays) and prompt applied field compensation compared to the existing SL01/10 sensor.

optimized design, with lower mutual coupling to the prompt applied fields, feedback using only the upper toroidal sensor array is found to be able to stabilize the mode up to $\beta_N = 4.7$ and correspondingly $C_\beta = 94\%$ without compensation of the applied fields. The result shows a remarkable advantage in control performance over the presently available device sensors (more than a twofold increase in C_β compared to the uncompensated SL01/10 sensor). It is also important to recognize the far greater mode amplitude found for the proposed sensor versus the SL01/10 pair, which will produce the higher signal to noise ratio required. Utilizing two toroidal sensor arrays at the upper and lower midplane can exhibit even higher performance close to the ideal with-wall limit of $C_\beta = 99\%$ with proper compensation of the applied prompt fields as is also shown in the figure. The same sensor design, implemented on the NSTX device, has produced a sufficient signal/noise to discriminate *n* values up to 3.[32] In addition to the increase in performance, utilizing a large number of sensors along the toroidal direction can be beneficial to cope with the possibility of the perturbed mode field changing helicity during active feedback.[31,39]

VII. CONCLUSIONS

Improved evaluation of global $n = 1$ active control performance in KSTAR includes expanded calculations using the present device sensors in the VALEN-3D code. The LM sensors can measure the radial field component of the RWM at the midplane where the ballooning nature of the mode is strongest, however, the nearby vessel currents induced by applied feedback are found to strongly limit the stabilization resulting in mode stabilization to 37% of the ideal MHD with-wall limit. The control performance of the off-axis saddle loops positioned at different poloidal locations inside the vacuum vessel is examined. The proximity to the RWM eigenfunction and the perturbation from the passive plates impact the performance of the saddle loops, and the SL01/10 sensor pair at the largest major radius region are found to be

adequate RWM control sensors which exhibit the highest control performance among the available device sensors. By utilizing a total number of 8 chosen saddle loops at the upper and lower midplane, the unstable $n = 1$ mode can be stabilized up to $\beta_N = 4.5$, corresponding to an obtainable C_β of 44%, and this can be increased to 86% by proper compensation of the prompt applied field. A transient feedback calculation using the chosen saddle loop sensors shows that growing modes can be actively stabilized with modest RMS control power, with higher power expectedly needed to get closer to the with-wall limit. Due to the low signal-to-noise ratio of the saddle loop sensors, the RWM can only be stabilized with a sensor white noise spectrum lower than 2 G. A new RWM sensor design motivated by the NSTX RWM B_p sensors is found to measure the mode perturbation with a greater signal-to-noise ratio and smaller coupling to the applied control fields and the induced vessel currents, and exhibits a remarkable improvement in performance over the existing device sensors, corresponding to mode stabilization nearly up to the ideal with-wall limit. The predicted control performance and power requirements are estimated without including initial mode rotation which generally improves RWM control. Therefore, the results shown here can be considered conservative regarding the control system requirements.

Future calculations may include further detail in the VALEN-3D model to better examine additional effects in feedback analysis, such as the addition of plasma rotation to the unstable plasma mode, and the impact on RWM stability by kinetic effects.[14] The addition of multiple plasma modes and a new model-based state space control technique[18] can improve the control capability in KSTAR by incorporating the effect of the full 3D wall eddy currents in real-time in future KSTAR experiments.

ACKNOWLEDGMENTS

[1] G. S. Lee, J. Kim, S. M. Hwang, C. S. Chang, H. Y. Chang, M. H. Cho, B. H. Choi, K. Kim, K. W. Cho, S. Cho *et al.*, Nucl. Fusion **40**, 575 (2000).

[2] M. Kwon, Y. K. Oh, H. L. Yang, H. K. Na, Y. S. Kim, J. G. Kwak, W. C. Kim, J. Y. Kim, J. W. Ahn, Y. S. Bae *et al.*, Nucl. Fusion **51**, 094006 (2011).

[3] O. Katsuro-Hopkins, S. A. Sabbagh, J. M. Bialek, H. K. Park, J. G. Bak, J. Chung, S. H. Hahn, J. Y. Kim, M. Kwon, S. G. Lee *et al.*, Nucl. Fusion **50**, 025019 (2010).

[4] J. G. Kwak, Y. K. Oh, H. L. Yang, K. R. Park, Y. S. Kim, W. C. Kim, J. Y. Kim, S. G. Lee, H. K. Na, M. Kwon *et al.*, Nucl. Fusion **53**, 104005 (2013).

[5] Y. S. Park, S. A. Sabbagh, J. M. Bialek, J. W. Berkery, S. G. Lee, W. H. Ko, J. G. Bak, Y. M. Jeon, J. K. Park, J. Kim *et al.*, Nucl. Fusion **53**, 083029 (2013).

[6] L. L. Lao, J. R. Ferron, T. S. Taylor, K. H. Burrell, V. S. Chan, M. S. Chu, J. C. Deboo, E. J. Doyle, C. M. Greenfield, R. J. Groebner *et al.*, Phys. Rev. Lett. **70**, 3435 (1993).

[7] Y. S. Park, S. A. Sabbagh, J. W. Berkery, J. M. Bialek, Y. M. Jeon, S. H. Hahn, N. Eidietis, T. E. Evans, S. W. Yoon, J.-W. Ahn *et al.*, Nucl. Fusion **51**, 053001 (2011).

[8] H. Jhang, J. Y. Kim, S. H. Ku, K.-I. You, and D. K. Lee, in proceedings of the 27th EPS Conference on Controlled Fusion and Plasma Physics (2000), Vol. 24B, p. 332.

[9] B. Hu and R. Betti, Phys. Rev. Lett. **93**, 105002 (2004).

[10]B. Hu, R. Betti, and J. Manickam, Phys. Plasmas **12**, 057301 (2005).

[11]B. Hu, R. Betti, and J. Manickam, Phys. Plasmas **13**, 112505 (2006).

[12]Y. Q. Liu, M. S. Chu, I. T. Chapman, and T. C. Hender, Phys. Plasmas **15**, 112503 (2008).

[13]Y. Q. Liu, M. S. Chu, I. T. Chapman, and T. C. Hender, Nucl. Fusion **49**, 035004 (2009).

[14]J. W. Berkery, S. A. Sabbagh, R. Betti, B. Hu, R. E. Bell, S. P. Gerhardt, J. Manickam, and K. Tritz, Phys. Rev. Lett. **104**, 035003 (2010).

[15]J. W. Berkery, S. A. Sabbagh, H. Reimerdes, R. Betti, B. Hu, R. E. Bell, S. P. Gerhardt, J. Manickam, and M. Podestà, Phys. Plasmas **17**, 082504 (2010).

[16]S. A. Sabbagh, J. W. Berkery, R. E. Bell, J. M. Bialek, S. P. Gerhardt, J. E. Menard, R. Betti, D. A. Gates, B. Hu, O. N. Katsuro-Hopkins *et al.*, Nucl. Fusion **50**, 025020 (2010).

[17]J. W. Berkery, S. A. Sabbagh, R. Betti, R. E. Bell, S. P. Gerhardt, B. P. LeBlanc, and H. Yuh, Phys. Rev. Lett. **106**, 075004 (2011).

[18]S. A. Sabbagh, J.-W. Ahn, J. Allain, R. Andre, A. Balbaky, R. Bastasz, D. Battaglia, M. Bell, R. Bell, P. Beiersdorfer *et al.*, Nucl. Fusion **53**, 104007 (2013).

[19]C. M. Bishop, Plasma Phys. Controlled Fusion **31**, 1179 (1989).

[20]Y. Q. Liu, A. Bondeson, C. M. Fransson, B. Lennartson, and C. Breitholtz, Phys. Plasmas **7**, 3681 (2000).

[21]C. M. Fransson, B. Lennartson, C. Breitholtz, A. Bondeson, and Y. Q. Liu, Phys. Plasmas **7**, 4143 (2000).

[22]A. Bondeson, Y. Q. Liu, C. M. Fransson, B. Lennartson, C. Breitholtz, and T. S. Taylor, Nucl. Fusion **41**, 455 (2001).

[23]M. Okabayashi, J. Bialek, M. S. Chance, M. S. Chu, E. D. Fredrickson, A. M. Garofalo, M. Gryaznevich, R. E. Hatcher, T. H. Jensen, L. C. Johnson *et al.*, Phys. Plasmas **8**, 2071 (2001).

[24]M. Okabayashi, J. Bialek, M. S. Chance, M. S. Chu, E. D. Fredrickson, A. M. Garofalo, R. Hatcher, T. H. Jensen, L. C. Johnson, R. J. La Haye *et al.*, Plasma Phys. Controlled Fusion **44**, B339 (2002).

[25]E. J. Strait, J. M. Bialek, I. N. Bogatu, M. S. Chance, M. S. Chu, D. H. Edgell, A. M. Garofalo, G. L. Jackson, R. J. Jayakumar, T. H. Jensen *et al.*, Phys. Plasmas **11**, 2505 (2004).

[26]S. A. Sabbagh, J. M. Bialek, R. E. Bell, A. H. Glasser, B. P. LeBlanc, J. E. Menard, F. Paoletti, M. G. Bell, R. Fitzpatrick, E. D. Fredrickson *et al.*, Nucl. Fusion **44**, 560 (2004).

[27]M. Okabayashi, J. Bialek, A. Bondeson, M. S. Chance, M. S. Chu, A. M. Garofalo, R. Hatcher, Y. In, G. L. Jackson, R. J. Jayakumar *et al.*, Nucl. Fusion **45**, 1715 (2005).

[28]P. R. Brunsell, D. Yadikin, D. Gregoratto, R. Paccagnella, Y. Q. Liu, T. Bolzonella, M. Cecconello, J. R. Drake, M. Kuldkepp, G. Manduchi *et al.*, Plasma Phys. Controlled Fusion **47**, B25 (2005).

[29]J. R. Drake, P. R. Brunsell, D. Yadikin, M. Cecconello, J. A. Malmberg, D. Gregoratto, R. Paccagnella, T. Bolzonella, G. Manduchi, L. Marrelli *et al.*, Nucl. Fusion **45**, 557 (2005).

[30]Y. Q. Liu, M. S. Chu, A. M. Garofalo, R. J. La Haye, Y. Gribov, M. Gryaznevich, T. C. Hender, D. F. Howell, P. de Vries, M. Okabayashi *et al.*, Phys. Plasmas **13**, 056120 (2006).

[31]S. A. Sabbagh, R. E. Bell, J. E. Menard, D. A. Gates, A. C. Sontag, J. M. Bialek, B. P. LeBlanc, F. M. Levinton, K. Tritz, and H. Yuh *et al.*, Phys. Rev. Lett. **97**, 045004 (2006).

[32]S. A. Sabbagh, A. C. Sontag, J. M. Bialek, D. A. Gates, A. H. Glasser, J. E. Menard, W. Zhu, M. G. Bell, R. E. Bell, A. Bondeson *et al.*, Nucl. Fusion **46**, 635 (2006).

[33]L. Marrelli, P. Zanca, M. Valisa, G. Marchiori, A. Alfier, F. Bonomo, M. Gobbin, P. Piovesan, D. Terranova, M. Agostini *et al.*, Plasma Phys. Controlled Fusion **49**, B359 (2007).

[34]E. Strumberger, P. Merkel, M. Sempf, and S. Günter, Phys. Plasmas **15**, 056110 (2008).

[35]H. K. Kim, H. L. Yang, G. H. Kim, J. Y. Kim, H. Jhang, J. S. Bak, and G. S. Lee, Fusion Eng. Des. **84**, 1029 (2009).

[36]J. M. Bialek, A. H. Boozer, M. E. Mauel, and G. A. Navratil, Phys. Plasmas **8**, 2170 (2001).

[37]S. G. Lee and J. G. Bak, Rev. Sci. Instrum. **72**, 439 (2001).

[38]A. H. Boozer, Phys. Plasmas **5**, 3350 (1998).

[39]M. Okabayashi, I. N. Bogatu, M. S. Chance, M. S. Chu, A. M. Garofalo, Y. In, G. L. Jackson, R. J. La Haye, M. J. Lanctot, J. Manickam *et al.*, Nucl. Fusion **49**, 125003 (2009).